Progress in Additive Manufacturing
https://doi.org/10.1007/s40964-024-00805-8

FULL RESEARCH ARTICLE

Stainless and low-alloy steels additively manufactured by micro gas metal arc-based directed energy deposition: microstructure and mechanical behavior

Paulo Henrique Grossi Dornelas[1] · Francisco Werley Cipriano Farias[1] · Tadeu C. da Silva[3,4] · João da Cruz Payão Filho[5] · A. S. Ramos[6] · J. P. Oliveira[1,2] · Telmo G. Santos[1,7]

Received: 29 May 2024 / Accepted: 14 September 2024

Abstract

Rising demands for miniaturization in industries such as aerospace and electronics have motivated advancements in metal additive manufacturing (AM), resulting in downscaled strategies using direct-energy deposition (DED) processes, now termed micro-DED (μ-DED). Within this context, micro gas metal arc DED (μ-GMA) has demonstrated the ability to deposit layers approximately 1 mm wide with a build rate of 30 cm^3/h, positioning this technology between GMA-based DED and other μ-DED processes in terms of regarding dimensional accuracy and build rate. Despite promising initial results, further evaluation of the process impact on the microstructure and mechanical behavior of various alloys is necessary due to the pioneering nature of μ-GMA. The present work focuses on the evaluation of the microstructure (via scanning electron microscopy, energy dispersive spectroscopy, thermodynamic simulations, and electron backscatter diffraction analyses) and mechanical behavior (using nanoindentation maps) of single-layer depositions of low alloy and stainless steels using μ-GMA. In addition, traditional GMA-based DED using larger diameter wires was employed to deposit comparably alloys for further discussion. μ-GMA successively deposited a low-alloy steel with a microstructure composed of ferrite and martensite–austenite constituents, achieving a nanohardness (NH) of 3.1 GPa and an elastic modulus (NE) of 196 GPa. In addition, μ-GMA additively manufactured stainless steel with a microstructure composed of a γ matrix and δ-ferrite, exhibiting an NH of 3.7 GPa and an NE of 188 GPa. These results for both deposited materials are comparable to those reported in the literature for regular GMA-based DED depositions, indicating that this new variant has promising potential as a printing technology for small and detailed parts.

Keywords Micro-additive manufacturing · Direct-energy deposition · Process downscaling

✉ Paulo Henrique Grossi Dornelas
p.dornelas@campus.fct.unl.pt

[1] UNIDEMI, Department of Mechanical and Industrial Engineering, NOVA School of Science and Technology, Universidade NOVA de Lisboa, 2829-516 Caparica, Portugal

[2] CENIMAT/I3N, Department of Materials Science, NOVA School of Science and Technology, Universidade NOVA de Lisboa, 2829-516 Caparica, Portugal

[3] Additive Manufacturing and Tooling Group, Federal University of Technology – Paraná, R. Deputado Heitor Alencar Furtado, 5000, Curitiba, PR 81280-340, Brazil

[4] LOM, Department of Mechanical Engineering, Fluminense Federal University, Niteroi RJ, Rio de Janeiro 24210-240, Brazil

[5] Metallurgical and Materials Engineering, Federal University of Rio de Janeiro (UFRJ), Rio de Janeiro, RJ 21941-972, Brazil

[6] CEMMPRE, Department of Mechanical Engineering, University of Coimbra, R. Luís Reis Santos, 3030-788 Coimbra, Portugal

[7] Laboratório Associado de Sistemas Inteligentes, LASI, 4800-058 Guimarães, Portugal

Published online: 27 September 2024

1 Introduction

Additive manufacturing (AM) is appointed as pivotal industrial technology due to its capacity to fabricate parts on demand with almost unrestricted geometric, as well as its capacity to be used in mass production [1]. Its cost-effectiveness for small-batch manufacturing [2] make it one of the pillars of Industry 4.0, which is possible due to the high level of automation and customization potential [3, 4]. AM facilitates rapid prototyping and part optimization [5, 6], proving to be a promising technology compared to milling and molding, particularly for complex design and customization [7, 8]. In addition, AM stands out as an environmentally friendly manufacturing technology, reducing material waste and promoting energy savings [9]. Among metal AM processes, it is possible to highlight powder bed fusion (PBF) [10] and directed energy deposition (DED) [8, 11] by their industrial scalability and technological maturation. Recently, there have been developments in DED processes to address the increasing needs for high-resolution and miniaturization, which are mainly influenced by the morphologic aspects of deposited layers (e.g., width and height). In this context, studies have been conducted to enhance DED resolution by downscaling the manufacturing setup, commonly referred to as μ-DED [12].

μ-DED processes are still considered a pioneering technology and have been relatively underexplored in the literature, presenting a promising field within the realm of AM. These technologies have been developed using a downscaling approach, which involves working with a smaller heat source and thinner filler metal. Horii et al. [13, 14] pioneered the development of a gas tungsten arc-based DED prototype, known as 3D micro-welding, designed to produce micro-scale metal components using micrometric wire and a pulsed micro-arc. This prototype utilized wire with a diameter of 200 µm and successfully deposited various materials, including pure metals (e.g., Ti), intermetallics (e.g., Ni–Al, Ti-Ni, Ti-Fe), austenitic alloys (e.g., Inconel 600, 304 stainless steel, and Invar 42), and compositionally graded materials [13–17]. 3D micro-welding showed promise due to the low heat input characteristic inherent to the gas tungsten arc process and its ability to process lower diameter wires. However, the extremely low deposition rate of this prototype can limit its applications. Jhavar et al. [18, 19] developed the micro-plasma transferred arc- wire deposition (μ-PTAWD). This μ-DED prototype was specifically designed for repairing defective dies and molds, as well as for constructing meso-sized, high-value components through precise layer deposition using Ø 300 µm wire. μ-PTAWD can achieve bead thicknesses smaller than 2000 µm and a deposition rate ranging from 5 to 50 cm^3/h [18]. In addition, issues related to discontinuities and lack of fusion (insufficient melting and bonding between layers) are typically reported, which are associated with improper process parameters (e.g., insufficient plasma power and excessive wire feed rate). Despite efforts to improve μ-PTAWD systems for accurate and smooth layer deposition, there is still a lack of results on printing workhorse alloys (e.g., stainless steels and non-ferrous based alloys) and their mechanical properties. Several authors have also employed the downscaling approach in laser-based DED. μ-laser melting deposition (μ-LMD) prototypes are capable of depositing thin layers (166 µm) and flawlessly constructing walls with an aspect ratio of up to 20 with a build rate of ~ 15 cm^3/h. They use a small wire diameter (as small as Ø = 0.1 mm) for various alloys (e.g., AISI 201, Resoloy, NiTi, and 304L stainless steel) [20–23]. The higher dimensional accuracy seen in the deposited parts originates from using a focused-energy heat source, setting it apart from other μ-DED technologies that depend on the electric arc, which possesses a larger heat-source dimension. In addition, the present authors conducted a comprehensive review (Dornelas et al. [12]), which address the state-of-the-art in micro-fabrication via μ-DED. This review encompasses existing μ-DED technologies, as well as a comparison of factors beyond process and deposited bead features, such as cost and environmental risks. Dornelas et al. reported the development of new systems based on a downscaling approach, which successfully achieved an increase in resolution and surface finishing, demonstrating that there is still room for the development and improvement of new technologies.

Recently, Dornelas et al. [24] developed a micro gas metal arc DED (μ-GMA) prototype, which combines the favorable characteristics of GMA-based DED, such as high build rates and low acquisition and operational costs, as well as a coaxial-feeding, which increases design freedom and resolution of the fabricated parts. The authors reported the technical feasibility of the μ-GMA prototype to deposit single-based multi-layer part (low alloy (LA) steel) with metallic bonding between the layers although the applied currents of deposition are typically around 30–40% below those used in (conventional) low-current GMA-based DED processes. In addition, the μ-GMA prototype showed the capability of depositing layers with an approximate width of 1 mm, nearly five times thinner than standard GMA-based DED, with a build rate of 30 cm^3/h. This approach presented a lower heat input (82 J/mm) and higher cooling rate (121 °C/s) than standard GMA-based DED operations.

Despite the promising initial results, the μ-GMA prototype represents pioneering work, and further efforts are needed to assess the mechanical and microstructural behavior of μ-GMA printed parts. In this context, to advance the

Table 1 Chemical composition (wt.%) of the filler metals

Material	Ø Wire (mm)	C	Mn	Si	Mo	Cr	Ni	Al	Nb + V + Ti	Fe
LA steel	0.30	0.01	0.58	0.86	< 0.01	0.09	0.06	1.13	0.05	Bal
ER80S-B2	1.00	0.09	0.55	0.48	0.55	1.35	0.10	–	< 0.01	Bal
ER316L	0.25	0.03	2.00	0.75	2.50	16.90	12.98	–	–	Bal
ER308L	1.00	0.03	1.83	0.56	0.10	18.40	9.44	–	0.09	Bal

Table 2 All-weld mechanical properties of the filler metals

Mechanical properties	Unity	ER80S-B2	ER308L	ER316L
Tensile strength	(MPa)	585	600	607
Yield strength	(MPa)	497	393	407
Elongation	(%)	22	34	35

understanding of the microstructure and mechanical behavior across a broader spectrum of materials, this work aimed to evaluate the microstructure and mechanical properties of LA, and stainless steels deposited by μ-GMA and compare them with those produced using conventional GMA-based DED technology. LA steel is commonly used in structural and engineering applications due to its favorable combination of strength, toughness, and weldability [25]. In addition, stainless steel is selected for its excellent corrosion resistance, mechanical properties, and versatility in various industrial sectors, including aerospace, automotive, and medical industries [26]. To characterize the deposited materials, the microstructure was assessed using scanning electron microscopy (SEM), energy dispersive spectroscopy (EDS), thermodynamic simulations, and electron backscatter diffraction (EBSD) analyses. The mechanical properties, such as hardness and Young's modulus (E), were evaluated through nanoindentation.

2 Experimental procedure

2.1 Material

A LA steel solid-wire with Ø 300 µm and a AISI 316L stainless steel solid-wire with Ø 250 µm were used as filler metals for μ-GMA depositions. For (conventional) GMA-based depositions, the solid-wire diameter was 1.0 mm for both materials. Hot-rolled 50 × 120 × 0.6 mm LA-steel plates were used as a substrate for μ-GMA, and 100 × 190 × 10 mm for GMA-based DED depositions. Before depositions, the substrates were ground with 80# sandpaper, cleaned with ethyl alcohol, and dried to avoid debris and oxidations. Table 1 depicts the wires' chemical composition, and Table 2 the all-weld mechanical properties. The inability to compare identical materials between μ-GMA and GMA-based DED stems from the current commercial unavailability of these materials in the form of micrometric wires.

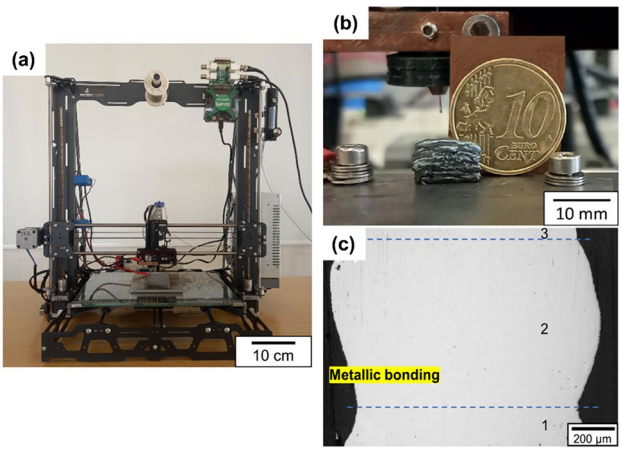

Fig. 1 **a** The μ-GMA prototype, **b** a 3D-printed 8-bead wall, and **c** its cross-sectional view showing the metallic bonding among the beads (adapted from reference [24])

2.2 Deposition apparatus

2.2.1 μ-GMA setup

The μ-GMA prototype is composed of a customized welding torch, a 3-axis moving table, and an electrical circuit associated to a Keithley 720 W bench power supply (as constant mode). The control of the 3-axis moving table and the wire feeding was performed using the Repetier Software® and an Arduino Mega 2560 microcontroller board. A detailed description of the μ-GMA prototype and its capabilities is available in reference [24]. Figure 1 shows an 8-bead wall deposited using the μ-GMA prototype with metallic bonding, demonstrating its feasibility.

2.2.2 GMA-based DED setup

GMA-based DED apparatus was composed by a customized welding torch mounted on a three-axis positioning system, a CITOWAVE III 520 welding power supply, and DMU W500 wire feeder, and control unit. This GMA-based DED machine was developed by the UNIDEMI research unit, and

its workability has been verified by the development of several works [6, 8, 27, 28].

2.2.3 Arc oscillogram measurements

Voltage and current curves from μ-GMA and GMA-based DED depositions were measured using a current transducer LEM HTA 600-S and a 14-bit ADC converter Digilent Analog Discovery 2 operating at 800 K samples/sec.

2.3 Direct-energy deposition

Depositions were performed using GMA-based DED and μ-GMA setups. The walls presented dimensions of 6.0 ± 0.1 mm and 1.1 ± 0.1 mm for width, 4.3 ± 0.1 mm and 2.3 ± 0.1 mm for height, and 10 mm and 100 mm for length for GMA-based DED and μ-GMA, respectively. The second bead for μ-GMA were deposited continuously, i.e., without a dwell time between the layers. It was not controlled because, in the first two passes, the temperature remained low due to the higher cooling rate, as no pre-heating was used. The interpass temperature for GMA-based DED was controlled at 150 °C, as indicated in material datasheet. The 2-bead walls were cross-sectioned, and the last pass was investigated, as shown in Fig. 2. The deposition parameters of GMA-based DED and μ-GMA are shown in Table 3.

2.4 Thermodynamic simulations

Thermodynamic simulations were performed in ThermoCalc® software using the TCFE12 and MOBFE7 thermodynamic databases. These simulations were used to predict the phases formation during solidification (Scheil-Gulliver model) and equilibrium diagram. The Scheil-Gulliver model considers a solid/liquid interface equilibrium, homogenous liquid, fast-diffusion interstitial elements (e.g., C), and minimal undercooling at dendrite tips. In addition, it was considered a typical cooling rate for GMA-based DED deposition (~ 10^2 K/s) [30].

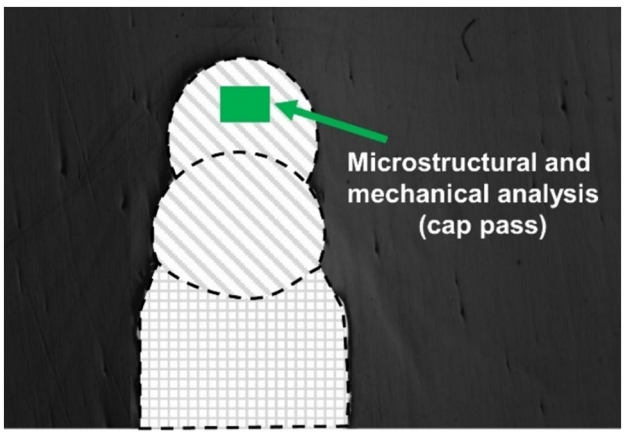

Fig. 2 Schematic drawing of the cross-sectional view of the deposited wall, indicating the region that was analyzed (cap pass)

Table 3 Process parameters of μ-GMA and GMA-based DED deposition

	μ-GMA	GMA-based DED
Voltage (V)*	13.0	17.0
Current (A)*	31.2	75.8
Heat input (J/mm)*	82	246
Polarity	DCEP	DCEP
CTWD (mm)	5	12
Shielding gas rate (l/min)	10	15
Travel speed (mm/s)	5	5
Wire feeding speed (mm/s)	120	66.7

*The voltage, current, and heat input were calculated through root-mean-square (RMS). For more details, refer to Scotti et al.[29]

2.5 Microstructural characterization

Samples for metallography were ground (with 100, 220, 320, 400, 500, 600, and 1200# sandpaper, sequentially) and polished (diamond paste with particle sizes of 3 and 1 µm, sequentially). The LA-steel microstructures were revealed through immersion etching in a solution containing 2 mL of nitric acid (HNO_3) in 98 mL of ethyl alcohol (CH_3CH_2OH) for 10 s, and the stainless steel samples in aqua regia in a molar ratio of 3:1 (HNO_3:HCL) for 20 s. SEM with a backscattered electron (BE) detector was performed using a Quanta 650 FEG. Samples for EBSD were prepared in the same way as the SEM ones, with an additional step of mechanical polishing in colloidal silica (SiO_2, 0.04 µm). EBSD analyses were performed using a Tescan Amber equipped with an energy dispersive X-ray (EDS) detector, with an accelerating voltage of 20 kV, a step size of 0.5 µm, and a working distance of 8 mm. Data post-processing was performed in MTEX [31].

2.6 Nanoindentation

The mechanical behavior of the LA and stainless steel beads deposited by μ-GMA were evaluated by nanoindentation in a Micro Materials—Nanohardness equipment (Berkovich diamond indenter). Hardness and reduced Young's modulus were determined by the Oliver and Pharr analysis method [32]. The nanoindentation experiments were run up to a maximum load of 6.2 mN. To obtain hardness and reduced Young's modulus maps from the center of the beads (Fig. 2), indentation matrixes with 8 rows and 12 columns

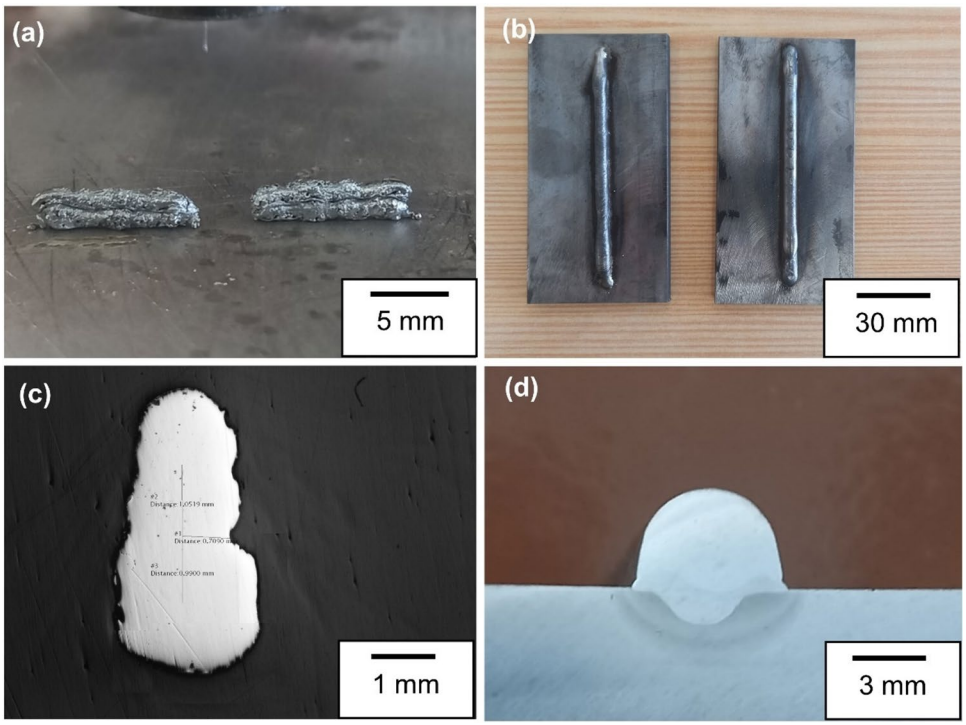

Fig. 3 Low alloy and stainless steel 2-bead walls deposited by **a** μ-GMA and **b** GMA-based DED, and a cross-sectional view of stainless steel deposited by **c** μ-GMA and **d** GMA-based DED

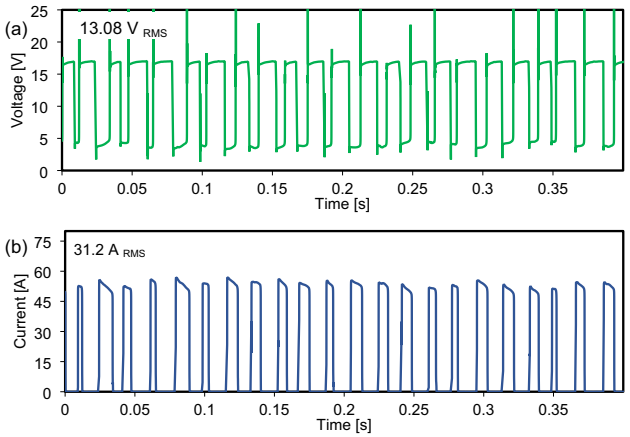

Fig. 4 **a** Voltage and **b** current curves during a μ-GMA deposition

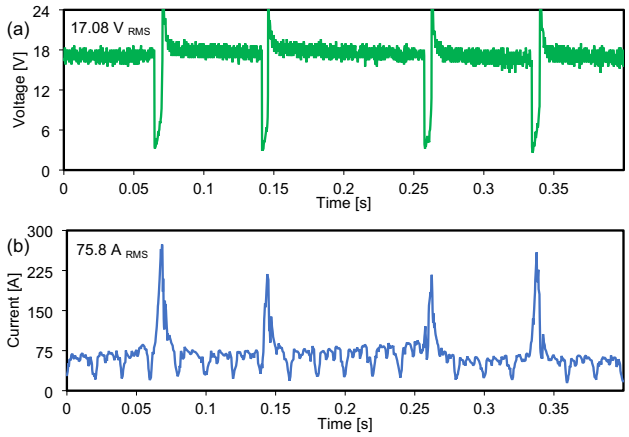

Fig. 5 **a** Voltage and **b** current curves during a GMA-based DED deposition

were defined (96 measurements). The distance between rows and columns was 15 and 10 µm, respectively.

3 Results and discussion

3.1 Direct-energy deposition

μ-GMA and GMA-based DED depositions were performed, and Fig. 3 shows the deposited walls and a cross-sectional view. Figures 4 and 5 illustrate V-I curves for μ-GMA and GMA-based DED depositions, respectively. Notice that, based on the V-I oscillograms of each process, the lower power of the μ-GMA is remarkable. The voltage and current were calculated through RMS. For more details, refer to Scotti et al. [29]. In addition, the frequency of the μ-GMA short-circuit transfer was about 60 Hz, which is higher than the 12 Hz of the GMA-based DED.

3.2 Microscopy

3.2.1 Stainless steel

Stainless steels may solidify in different modes according to its chemical composition and cooling rate [33]. It is well known that the solidification mode of austenitic stainless steel depends on the Cr_{eq} and Ni_{eq} content, which can be estimated (Equations I and II, respectively) using the Welding Research Council (WRC-1992) formulas. Hence, depending on the ratio of Cr_{eq}/Ni_{eq}, stainless steel can undergo solidification in four distinct modes [34, 35]: austenite (A), austenite–ferrite (AF), ferrite–austenite (FA), and ferrite (F) modes. Equations III, IV, V, and VI represent the A, AF, FA, and F solidification modes, where L, δ, and γ refer to liquid, high-temperature ferrite, and austenite phases, respectively.

$$Cr_{eq} = Cr + Mo + 0.7Nb \quad (1)$$

$$Ni_{eq} = Ni + 35C + 20N + 0.25Cu \quad (2)$$

$$\text{A mode } L \rightarrow L + \gamma \rightarrow \gamma \quad Cr_{eq}/Ni_{eq} < 1.37 \quad (3)$$

$$\text{AF mode } L \rightarrow L + \gamma \rightarrow L + \gamma + \delta \rightarrow \gamma + \delta \quad 1.37 < Cr_{eq}/Ni_{eq} < 1.5 \quad (4)$$

$$\text{FA mode } L \rightarrow L + \delta \rightarrow L + \gamma + \delta \rightarrow \delta + \gamma \quad 1.5 < Cr_{eq}/Ni_{eq} < 2.0 \quad (5)$$

$$\text{F mode } L \rightarrow L + \delta \rightarrow \delta + \gamma \quad Cr_{eq}/Ni_{eq} > 2.0 \quad (6)$$

Figure 6a shows micrographs of the 316L stainless steel deposited by μ-GMA with a microstructure composed of δ-ferrite within a cellular austenitic grains matrix. The cellular structure is generally attributed to the high cooling rate, which induces non-equilibrium solidification conditions, as occurred for fast solidification processes (e.g., laser-based DED processes) [36]. According to Equations I and II, Cr_{eq}/Ni_{eq} calculated for 316L is 1.38 (wire composition, Table 1), which indicates that solidification occurs in the AF mode This mechanism is characterized by solidification as primary austenite ($L \rightarrow L + \gamma$). As solidification progresses, austenite grows, segregation ferrite-former elements such as Cr and Mo to the sub-grain boundaries/interdendritic region [33]. Thus, the solid/liquid interface becomes richer in ferrite-promoting elements, allowing some δ-ferrite to form via a eutectic reaction ($L \rightarrow \beta + \gamma$) at the end of the primary solidification. In other words, due to the redistribution of elements, the Cr_{eq}/Ni_{eq} ratio changes at the interdendritic region as solidification advances, which can alter the solidification mode (e.g., from A to AF). Thus, the product of solidification AF mode is $\delta + \gamma$. EDS analyses (Fig. 7a, Table 4) show a segregation of Cr and Mo at the dendrite boundaries with a $Cr_{eq}/Ni_{eq} = 2.15$ (F mode, Equation VI), which confirms the described mechanisms. The primary austenite solidification was supported predicted by Scheil-Gulliver simulation (Fig. 8a), and the following described reactions (AF mode) were supported by equilibrium phase diagram simulation (Fig. 8c). In addition, the AF mode for 316L is in line with WRC 1992 diagram (Fig. 9). Several authors have reported 316L solidification during GMA-based DED depositions occurring in the AF mode [28, 37, 38]. In addition, some laser-based AM studies have indicated the suppression of δ-ferrite formation during solidification (i.e., A mode)

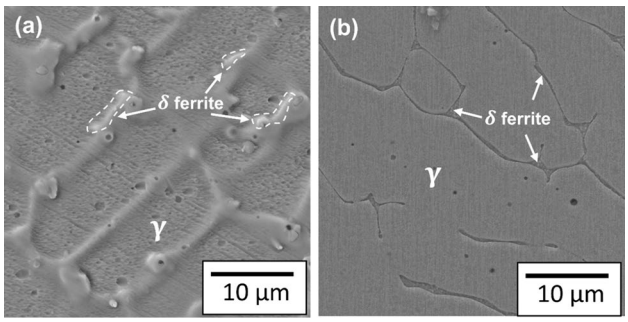

Fig. 6 Scanning electron microscopy of stainless steel deposited by **a** μ-GMA, and **b** GMA-based DED

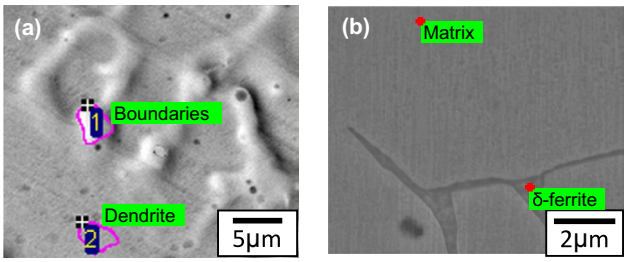

Fig. 7 Exact location where energy dispersive spectroscopy was performed for stainless steel deposited by **a** μ-GMA and **b** GMA-based DED

Table 4 Semi-quantitative analysis performed by energy dispersive spectroscopy in the 316L and 308 stainless-steel samples following Fig. 6 indicated area

Elements	316L		308	
	1. Boundaries	2. Dendrite (γ)	3. δ-ferrite	4. Matrix (γ)
Fe	64.67	71.37	65.94	67.98
Cr	18.28	15.51	26.48	19.91
Ni	10.43	9.68	4.77	9.38
Mo	4.22	1.78	-	-
Mn	1.05	0.71	1.74	1.90
Al	0.69	0.46	0.86	0.65
Si	0.67	0.50	0.22	0.19

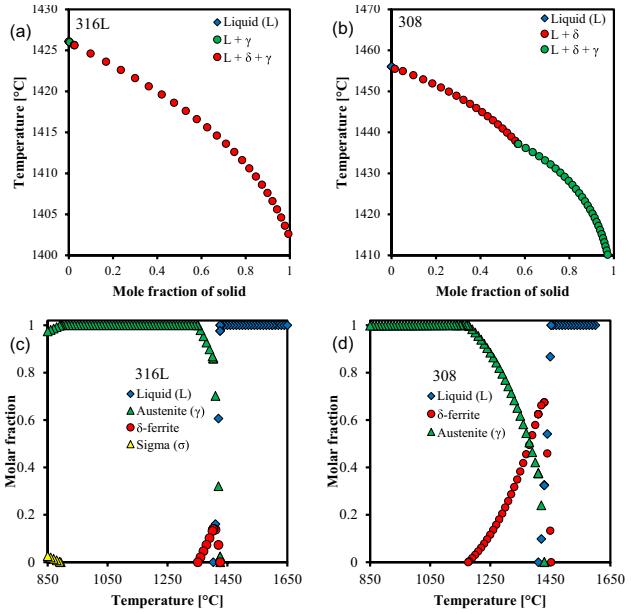

Fig. 8 **a** and **b** Scheil-Gulliver, and **c** and **d** equilibrium-phase diagram simulations for 316L and 308 stainless steels, respectively

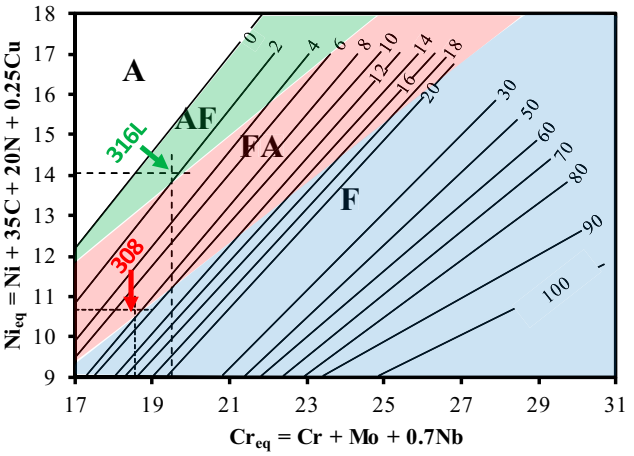

Fig. 9 Solidification modes according to Cr_{eq} and Ni_{eq} content (adapted from Welding Research Council 1992 diagram)

[39–43] due to higher cooling rates. A fast-cooling rate can reduce the diffusibility of ferrite-forming elements in the dendritic boundaries at elevated temperatures, allowing the A mode to remain stable throughout the entire solidification sequence.

Figure 6b display micrographs of the 308 stainless steel ($Cr_{eq}/Ni_{eq} = 1.76$) deposited by conventional gas metal arc-based GMA-based DED, which exhibited a microstruture composed by a γ matrix and δ-ferrite. According to Equation V, the solidification occurred as primary ferrite (FA mode). In this mechanism, primary ferrite is initially precipitated from the molten metal ($L \rightarrow L + \delta$), which was facilitated by the presence ferrite stabilization elements, e.g., Cr, Mo, Si, Ti, and Nb. As the primary ferrite (δ-ferrite) solidification approaches the end, the formation of the austenite phase starts at the boundaries of cellular grains/columnar dendrites of ferrites through peritectic/eutectic reactions ($L + \delta \rightarrow \gamma; L \rightarrow \gamma + \delta$) [33]. Moreover, due to the rapid cooling process, δ-ferrite remains at room temperature because the $\delta \rightarrow \gamma$ phase transformation was not completed. These residual ferrite remnants persist at the grain boundaries of austenite at room temperature, as shown in Fig. 6b. Therefore, the final microstructure is composed of austenite and δ-ferrite (enriched with ferrite-former elements), which is in line with GMA-based DED and arc-based welding literature [33, 44–47]. EDS analyses proved the difference in the content of ferrite-former elements between the center of the dendrites and the δ-ferrite (Fig. 7b, Table 4). In addition, the FA-solidification mode was predicted by Scheil-Gulliver simulation (Fig. 8b), and the following described reactions were confirmed by equilibrium-phase diagram simulation (Fig. 8d). Although the WRC-1992 diagram (Fig. 9) is a powerful tool developed to predict the conventional weld-metal microstructures (lower cooling rates in relation to additive manufacturing) [42, 43], this diagram was also able to predict and support the previously described solidification mechanisms for both 308 (GMA-based DED) and 316L (μ-GMA) stainless steels.

A typical issue related to additively manufactured non-allotropic alloys (e.g., stainless steel and Ni-based superalloys) lies in a coarse and oriented microstructure (crystallographic texture) due to the epitaxial growth

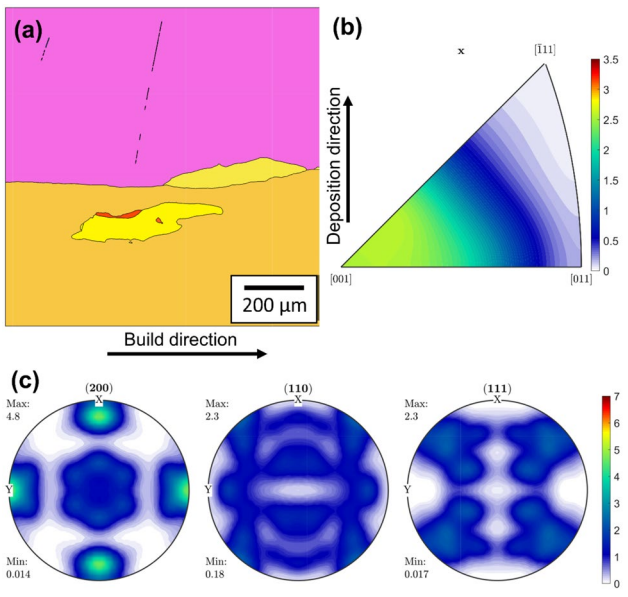

Fig. 10 Electron backscatter diffraction **a** orientation image map, **b** inverse pole figure, and **c** pole figure of the 316L stainless steel deposited by μ-GMA

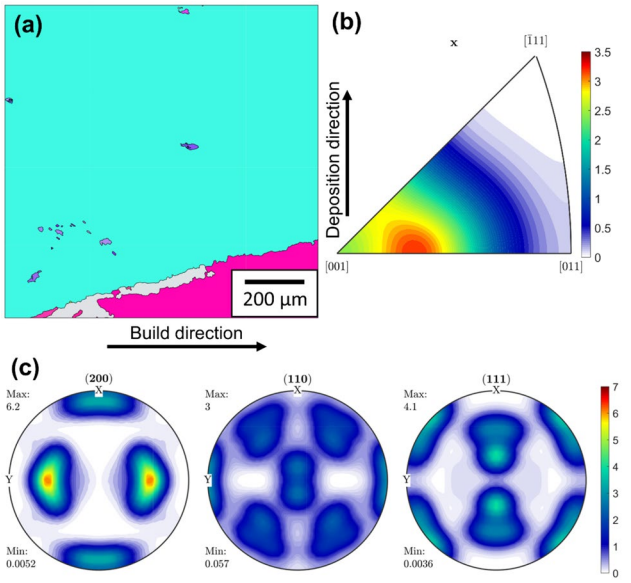

Fig. 11 Electron backscatter diffraction **a** orientation image map, **b** inverse pole figure, and **c** pole figure of the 308 stainless steel deposited by GMA-based DED

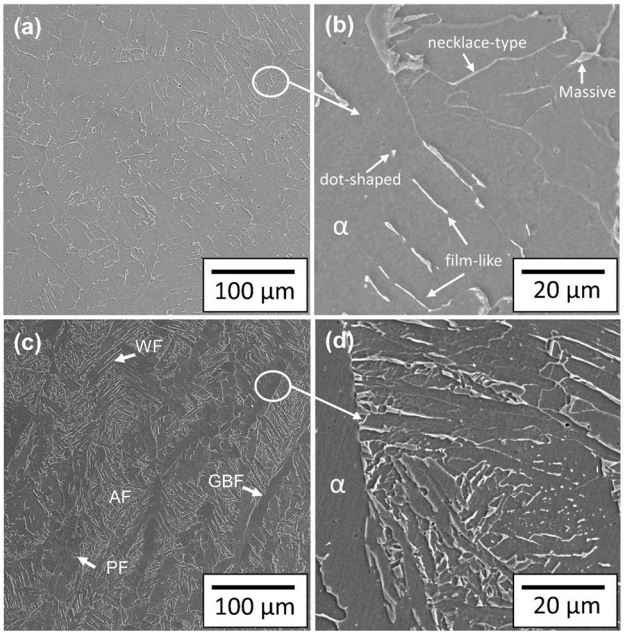

Fig. 12 Scanning electron microscopy of low alloy steel deposited by **a**–**b** μ-GMA, and **c**–**d** GMA-based DED

and layer-by-layer process aspect [48]. This can result in inferior and anisotropic mechanical and physical properties, jeopardizing the components' performance [49–51]. Figures 10 and 11 show EBSD analyses performed in μ-GMA and GMA-based DED samples respectively, which indicated that, independently of the 3D priting process (μ-GMA or GMA-based DED), the grains are coarse (millimetric-sized) and oriented (columnar aspect) in relation to the building direction. In addition, their respective pole figures and inverse pole figures indicated that μ-GMA and GMA-based DED had a cubic-based oriented microstructure. μ-GMA showed a clear moderated cube ($\{100\}<100>$) texture, while GMA-based DED exhibited a rotated cube ($\{100\}<110>$) and cube ($\{100\}<100>$) texture aspects. These texture aspects were related to the easy growth direction and planes for body-centered and face-centered metals ($<100>$ and $\{100\}$, respectively). Due to the epitaxy and competitive growth on the melting pool, the grains with the easy growth direction and planes alligned to building direction (maximum heat flux) hinder the slower grains, which originated the typical cubic-based texture observed in fusion-based additively manufactured body-centered and face-centered metals [52–54]. Furthermore, μ-GMA exhibits a less oriented microstructure compared to GMA-based DED, which can be attributed to the lower heat input (82 J/mm) and, consequently, a faster cooling rate (according to Rosenthal's equation [55]), leading to a finer and less oriented microstructure.

3.2.2 Low alloy steel

Figure 12a and b display micrographs of the LA-steel deposited by μ-GMA, which had a microstruture composed by a α ferrite matrix with martensite–austenite (*M*–*A*) constituents. The observed *M*–*A* constituents have different morphologies as dot-shaped (dispersed within the α matrix), film-like (occurring within α grains), necklace-type (characterized by occurrences along the boundaries of α grains), and massive *M*–*A*. The latter was distinguished by a core–shell structure, where martensite forms the outer region (shell), and austenite constitutes the inner region (core) [56]. As previosly described, the wires' chemmical composition used for μ-GMA was not designed for welding/additive manufacturing applications. As shown in Table 1, the chemical composition of the micrometric wire is almost pure Fe (98% Fe) with a relevant Al content (1.13%), which serves as an oxidation inhibitor. In this case, during solidification, the austenite transformed into ferrite segregating carbon to the grain boundaries. These carbon-enriched γ islands transform into cementite (Fe_3C) or promote the formation of *M*–*A* constituents. However, besides the high cooling-rates characteristic of μ-GMA deposition contributes to the *M*–*A* formation [56–59], the Al content delays the formation of Fe_3C, which also contributed to the *C*-enriched islands which subsequently transforms into *M*–*A* [60]. Figure 12c and d show a typical microstructural arrangement of the cap pass of a HSLA steel deposition, which is composed of columnar

grains (the columnar morphology is easier to notice in the EBSD map), with different ferrite morphologies.

HSLA steels initially solidify as δ-ferrite (~ 1540 °C) and then transform into austenite (γ) phase (~ 1450 °C) in a solid-state reaction. When the solidification temperature reaches values below the A_3 temperature, allotriomorphic ferrite is the first phase to form, which nucleates heterogeneously at the boundaries of austenite columnar grains, and then forms layers that follow the grain boundary contours [61]. Allotriomorphic ferrite is also referred to as proeutectoid or grain boundary ferrite (GBF). Polygonal ferrite (PF) can nucleate at the boundary and within the austenite grains at lower cooling rates; at higher cooling rates, ferrite can nucleate at the GBF and grow as Widmanstäetten pattern (WF) into the austenitic grain. The remaining austenite within the grain will transform into an acicular ferrite (AF) at lower temperatures by displacive transformations [61]. The formation of GBF, WF, PF, and AF are indicated in the Fig. 12c.

Figures 13 and 14 show EBSD analysis performed in μ-GMA and GMA-based DED LA steel samples, respectively. As previously demonstrated in Fig. 12, μ-GMA microstructure is formed predominantly by ferrite, which is also observed in EBSD analyses, which did not present a preferential orientation (i.e., non-oriented microstructure). Despite the majority of additively manufactured metals showing an oriented microstructure, such as stainless steels (refer to Figs. 10 and 11), solid-state transformation alloys, especially the LA steels, typically do not show an oriented microstructure due to their double solid-state transformation ($\delta \rightarrow \gamma$ and $\gamma \rightarrow \alpha$) during thermal cycling. Similar to μ-GMA, the GMA-based DED samples did not show an orientated microstructure. In addition, it was verified the existence of two distintic regions, the as-deposited material and the heat-affected zone, which showed a significant difference in grain size and morphology. This stems from the reheating thermal cycle (subsequently layer deposition), which reaustenitized the previous layer, refining the prior austenite grain size and consequently the parent phase (α). These results, i.e., absence of preferential orientation for both μ-GMA and GMA-based DED, are per the previous one presented in the literature [62, 63].

3.3 Mechanical properties

The nanoindentation test is frequently employed for assessing local mechanical properties, enabling the measurement of both hardness (NH) and elastic modulus (NE) at a micrometer or nanometer scale. Due to the limited cross-sectional dimensions of the specimens, it was impractical

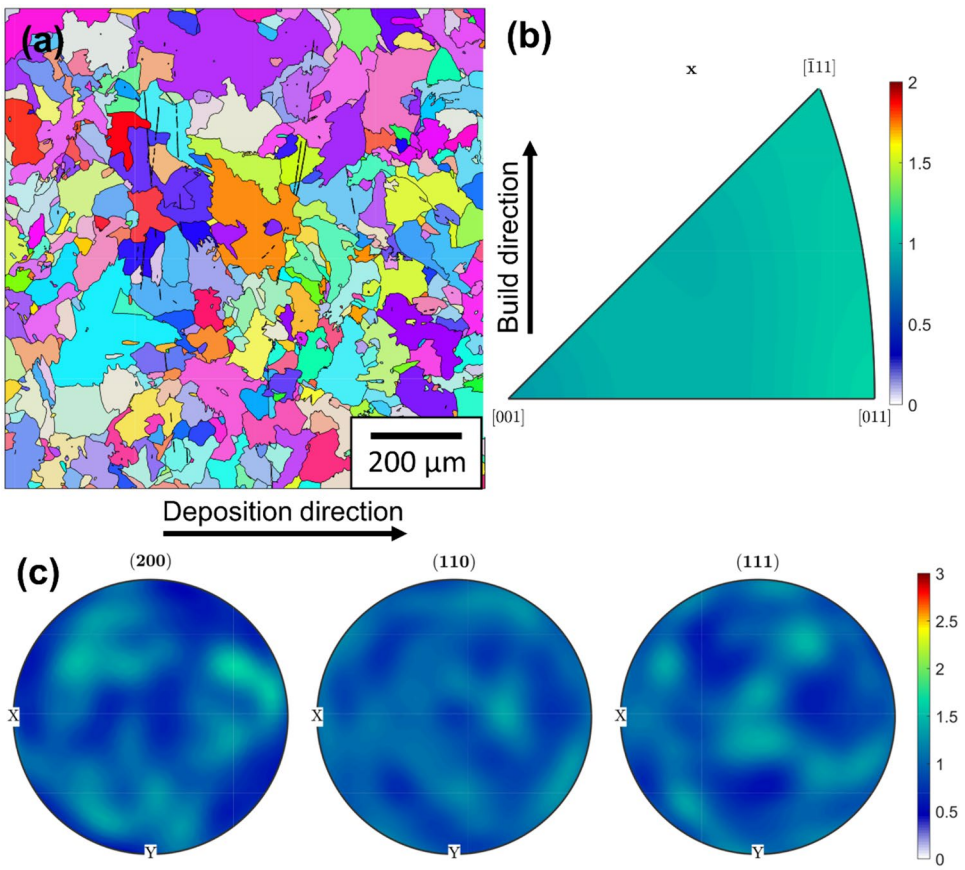

Fig. 13 Electron backscatter diffraction **a** orientation image map, **b** inverse pole figure, and **c** pole figure of the low alloy steel deposited by μ-GMA

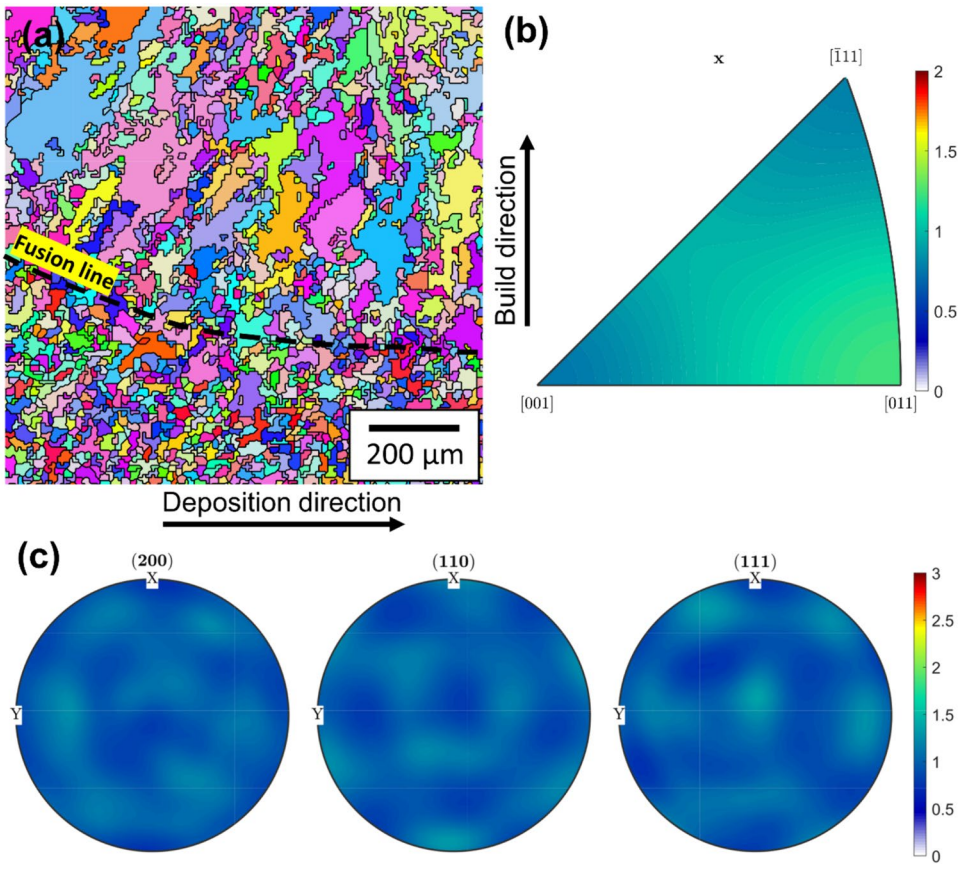

Fig. 14 Electron backscatter diffraction **a** orientation image map, **b** inverse pole figure, and **c** pole figure of the low alloy steel deposited by GMA-based DED

and nearly unfeasible to fabricate conventional tensile specimens, even subsidized, to obtain typical strength (yield and ultimate tensile) and Young's modulus results. Therefore, nanoindentation tests were adopted as an alternative and effective approach. Here, nanoindentation maps were performed in both LA steel and stainless steel μ-GMA samples.

Figure 15a and b show nanoindentation hardness maps of the LA and stainless and steel. For the LA steel, the NH values vary between 2.0 and 4.1 GPa, with an average value of 3.1 GPa (Fig. 16a). According to the literature, the ferrite's NH of LA steel is around 2.2–3 GPa (steel with 0.05–0.07%C) [64]. Thus, it is reasonable to establish that these islands with NH > 3.5 GPa represent *M–A* constituent's formation, as identified from microscopy observations (Fig. 12). This result is supported by literature data which reports martensite NH values in LA steel around 3 to 4 GPa [65]. On the other hand, the NH map of the stainless steel (Fig. 15) showed an average value of 3.7 GPa (Fig. 16b) from values in the range of 2.1–4.9 GPa, which corresponds to the fully austenitic matrix. Notice a region on the left side of the map with NH values higher than 4 GPa. This difference corresponds to an interdendritic region, which can exhibit higher values due to certain solidification phenomena such as impurity concentration and solid solution hardening caused by the enrichment of alloying elements (as discussed previously). This last mechanism is stimulated due to the higher cooling rate characteristic of the μ-GMA, once it restricts atomic diffusibility. The NH value found is in line with other works which reported austenite NH values between 3 and 4 GPa [66].

Figure 17a and b show NE maps of the LA and stainless steel, respectively. For the LA steel, E map showed an average value of 188.2 GPa (Fig. 18a), which is in line with GMA-based DED works available in literature (Table 5). This result is expected since the E is significantly influenced by crystallographic aspects [67]. Tankova et al. [68] studied the mechanical properties of carbon steel coupons produced by CMT-GMA-based DED and reported $E = 214$ GPa. Ermakova et al. [69] reported E between 181 and 221 GPa for LA-steel components produced by GMA-based DED. Lagui et al. [70] also reported E values of 200–210 GPa for carbon steel plates produced by GMA-based DED. For the stainless steel, Fig. 18b shows that the average NE obtained was 196 GPa. This result is also comparable with stainless steel GMA-based DED works available in the literature. Gordon et al. [71] studied anisotropy of stainless-steel wall printed by GMA-based DED and reported E values between 130 and 140 GPa. Zhao et al. [72] developed a comprehensive series of tensile tests on 316L stainless steel deposited by GMA-based DED under different conditions of heat

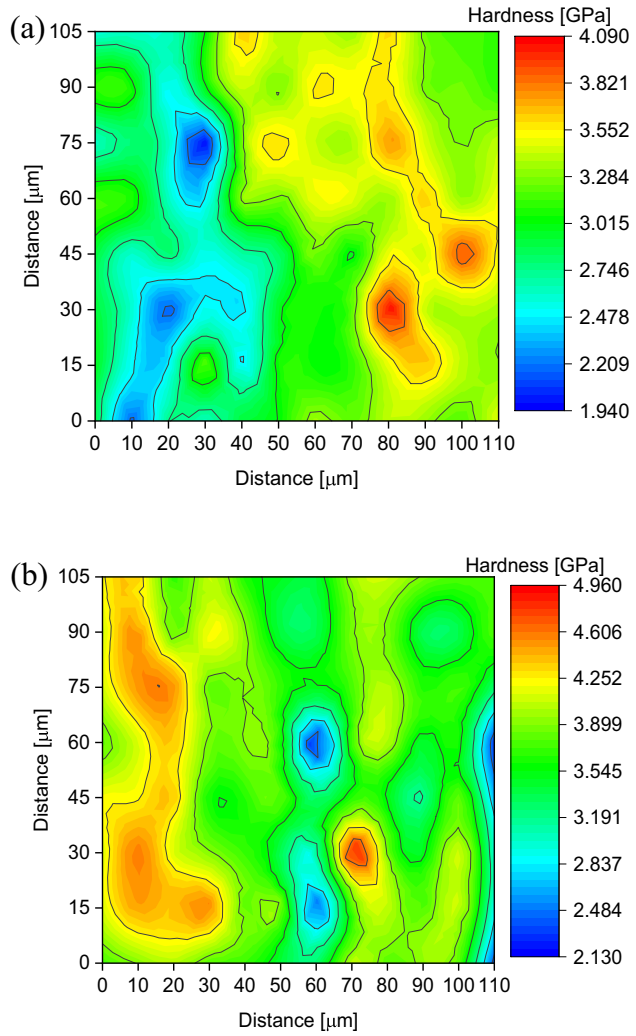

Fig. 15 Nanohardness map of the **a** low alloy steel and **b** 316L stainless steel μ-GMA sample

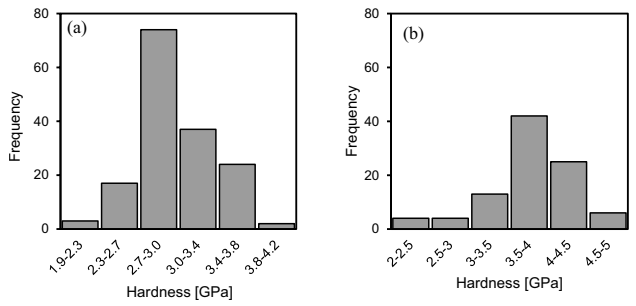

Fig. 16 Frequency distribution of the hardness measurements of the **a** low alloy steel and **b** 316L stainless steel μ-GMA sample

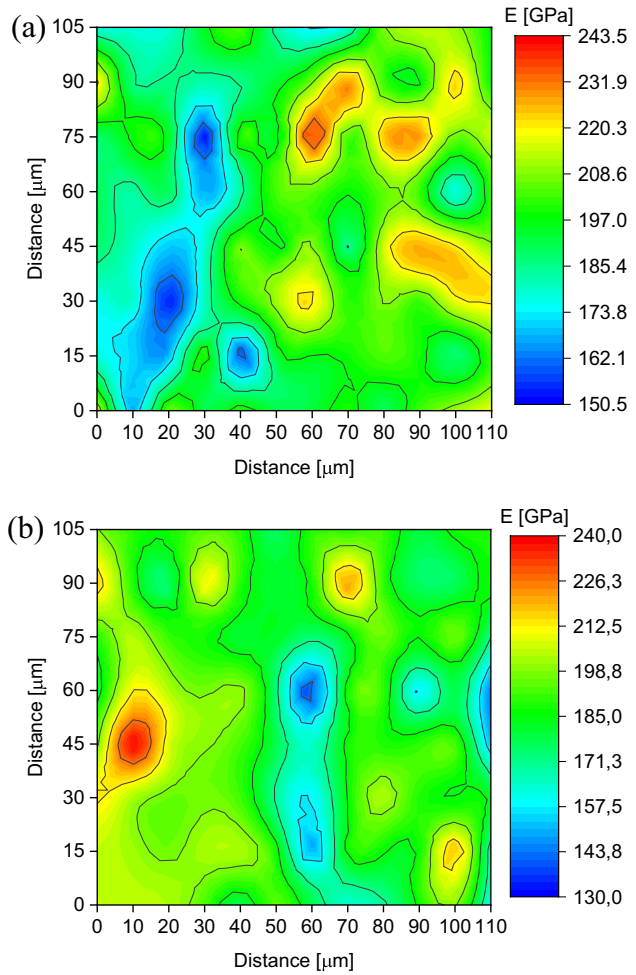

Fig. 17 **a** Reduced Young's modulus map of the **a** low alloy steel and **b** 316L stainless steel μ-GMA sample

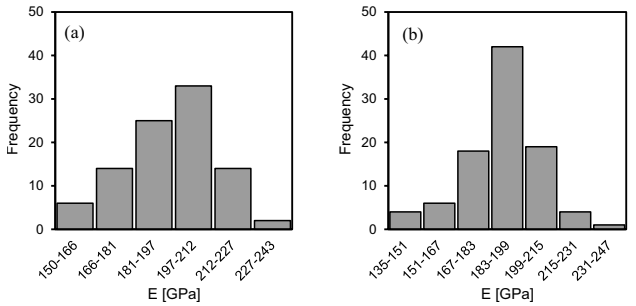

Fig. 18 Frequency distribution of the reduced Young's modulus measurements of the **a** low alloy and **b** 316L stainless steel sample

treatment and reported E values between 139 and 191 GPa [72]. In addition, the obtained NE is close to the conventional wrought material (about 190 GPa) [73].

Considering the material limitations for this work, using only two stainless steels with different Cr/Ni ratios, LA steel, and Fe-based microwires does not provide a complete picture of how the microstructure and properties change when the same alloys are processed by μ-GMA and GMA-based

Table 5 Literature data on Young's modulus (E) obtained from GMA-based DED depositions of low alloy (LA) and stainless steels (SS) and the measured values from μ-GMA depositions

Material	Authors	E (GPa)	Refs.
LA	μ-GMA	196	–
	Tankova et al	214	[68]
	Ermakova et al	181–221	[69]
	Lagui et al	200–210	[70]
	Yoshinaga et al.*	214–232	[74]
SS	μ-GMA	188	–
	Gordon et al	130–140	[71]
	Zhao et al	139–191	[72]
	Colin et al.*	190	[73]

*Wrought material

DED. However, some points can still be explored. In the case of LA steels, beads deposited by both processes exhibited a microstructure consisting of a ferritic matrix with the presence of *M–A* constituents and carbides. The difference that can be pointed out is the coarser ferrite microstructure of the μ-GMA than conventional GMA-based DED. Although the last has higher heat input, this morphologic difference between them is attributed mainly to the variation in the chemical composition. Both stainless steel microstructures are composed of austenite and delta ferrite; however, they were formed through different solidification mechanisms. These mechanisms were also controlled by the difference in chemical composition between the two processes rather than the cooling rate. Nevertheless, the latter led to the formation of a cellular structure in μ-GMA, in which this morphology is not characteristic of conventional GMA-based DED. In addition, regardless of the solidification mode and process, the tested stainless steels exhibited a coarse and oriented microstructure. To achieve a more comprehensive understanding, future research will include a wider variety of materials with similar compositions. However, these preliminary results indicate that μ-GMA can satisfactorily deposit LA and stainless steel parts, achieving mechanical properties and microstructures comparable to those obtained by conventional GMA-based DED.

4 Conclusions

This work developed a comparative analysis of the microstructural and mechanical behavior of austenitic stainless and LA steel deposited by μ-GMA (prototype) and GMA-based DED (consolidated) technologies. The microstructure was assessed through thermodynamic simulation, SEM and EBSD analysis, while nanohardness and reduced Young's modulus were determined from nanoindentation maps. The following conclusions were drawn:

- The 316L stainless steel deposited by μ-GMA showed a microstructure composed of δ-ferrite within an austenitic matrix, resulting from solidification in the AF mode. In contrast, 308 stainless steel deposited by conventional gas metal arc-based DED exhibited a microstructure composed of a γ matrix and δ-ferrite from solidification in the FA mode. EDS analyses and thermodynamic simulations confirmed these solidification mechanisms. In addition, preferential orientation was observed for both μ-GMA and GMA-based DED microstructures.
- LA steel deposited by μ-GMA had a microstructure composed of an α ferrite matrix with *M–A* constituents. In contrast, the LA steel deposited by conventional gas metal arc-based DED had a typical microstructural arrangement of the cap pass composed of columnar grains with different ferrite morphologies. Absence of preferential orientation was observed for both μ-GMA and GMA-based DED microstructures.
- Nanoindentation hardness maps of the LA and stainless steel showed average values of 3.1 and 3.7 GPa, respectively. In addition, Reduced Young's modulus maps showed average values of 196.6 and 188.2 GPa for the LA and stainless steel, respectively. These values align with similar materials deposited by conventional GMA-based DED technologies.
- μ-GMA technique exhibits the capability to deposit LA and stainless-steel walls with mechanical properties comparable to those achieved through conventional GMA-based DED depositions. This underscores the promising potential of μ-GMA as a viable and effective deposition technique for such materials.

Funding Open access funding provided by FCT|FCCN (b-on). Authors acknowledge the Portuguese Fundação para a Ciência e a Tecnologia (FCT—MCTES) for its financial support via the project UIDB/00667/2020 and UIDP/00667/2020 (UNIDEMI). P. H. G. Dornelas acknowledges FCT—MCTES for funding the PhD grant 2021.05298.BD. F. W. C. F acknowledges FCT-MCTES for funding the Ph.D. Grant 2022.13870.BD. JPO acknowledges funding by national funds from FCT—Fundação para a Ciência e a Tecnologia, I.P., in the scope of the projects LA/P/0037/2020, UIDP/50025/2020 and UIDB/50025/2020 of the Associate Laboratory Institute of Nanostructures, Nanomodelling and Nanofabrication—i3N. This research is sponsored by national funds through FCT—Fundação para a Ciência e a Tecnologia, under projects UIDB/00285/2020 and LA/P/0112/2020. This activity has received funding from the European Institute of Innovation and Technology (EIT) RawMaterials through the project Smart WAAM: Microstructural Engineering and Integrated Non-Destructive

Testing. This body of the European Union receives support from the European Union's Horizon 2020 research and innovation programme.

Declarations

Conflict of interest The authors declare no conflict of interest.

References

1. Shukla M, Todorov I, Kapletia D (2018) Application of additive manufacturing for mass customisation: understanding the interaction of critical barriers. Prod Plan Control 29:814–825. https://doi.org/10.1080/09537287.2018.1474395
2. Thomas DS, Gilbert SW (2014) Costs and Cost Effectiveness of Additive Manufacturing. Gaithersburg, MD
3. Sepasgozar SME, Shi A, Yang L et al (2020) Additive manufacturing applications for industry 4.0: a systematic critical review. Buildings 10:231. https://doi.org/10.3390/buildings10120231
4. Haleem A, Javaid M (2019) Additive manufacturing applications in industry 4.0: a review. J Ind Integr Manag 04:1930001. https://doi.org/10.1142/S2424862219300011
5. Chua CK, Chou SM, Wong TS (1998) A study of the state-of-the-art rapid prototyping technologies. Int J Adv Manuf Technol 14:146–152. https://doi.org/10.1007/BF01322222
6. Farias FWC, Duarte VR, Felice IO et al (2023) In situ interlayer hot forging arc plasma directed energy deposition of Inconel® 625: microstructure evolution during heat treatments. J Alloys Compd 952:170059. https://doi.org/10.1016/j.jallcom.2023.170059
7. Gurr M, Mülhaupt R (2016) Rapid Prototyping. In: Reference Module in Materials Science and Materials Engineering. Elsevier
8. Cipriano Farias FW, Rebelo Duarte V, da Cruz Payão Filho J et al (2024) Arc-based directed energy deposited Inconel 718: role of heat treatments on high-temperature tensile behavior. Mater Res Lett 12:97–107. https://doi.org/10.1080/21663831.2023.2297734
9. Lee H, Lim CHJ, Low MJ et al (2017) Lasers in additive manufacturing: a review. Int J Precis Eng Manuf Green Technol 4:307–322. https://doi.org/10.1007/s40684-017-0037-7
10. Dev Singh D, Mahender T, Raji Reddy A (2021) Powder bed fusion process: a brief review. Mater Today Proc 46:350–355. https://doi.org/10.1016/j.matpr.2020.08.415
11. Svetlizky D, Das M, Zheng B et al (2021) Directed energy deposition (DED) additive manufacturing: physical characteristics, defects, challenges and applications. Mater Today 49:271–295. https://doi.org/10.1016/j.mattod.2021.03.020
12. Dornelas PHG, Santos TG, Oliveira JP (2022) Micro-metal additive manufacturing–state-of-art and perspectives. Int J Adv Manuf Technol 122:3547–3564. https://doi.org/10.1007/s00170-022-10110-9
13. Horii T, Kirihara S, Miyamoto Y (2009) Freeform fabrication of superalloy objects by 3D micro welding. Mater Des 30:1093–1097. https://doi.org/10.1016/j.matdes.2008.06.033
14. Horii T, Kirihara S, Miyamoto Y (2008) Freeform fabrication of Ti–Al alloys by 3D micro-welding. Intermetallics (Barking) 16:1245–1249. https://doi.org/10.1016/j.intermet.2008.07.009
15. Terakubo M, Oh J, Kirihara S et al (2007) Freeform fabrication of Ti–Ni and Ti–Fe intermetallic alloys by 3D micro welding. Intermetallics (Barking) 15:133–138. https://doi.org/10.1016/j.intermet.2006.03.012
16. Katou M, Oh J, Miyamoto Y et al (2007) Freeform fabrication of titanium metal and intermetallic alloys by three-dimensional micro welding. Mater Des 28:2093–2098. https://doi.org/10.1016/j.matdes.2006.05.024
17. Terakubo M, Oh J, Kirihara S et al (2005) Freeform fabrication of titanium metal by 3D micro welding. Mater Sci Eng A 402:84–91. https://doi.org/10.1016/j.msea.2005.04.025
18. Jhavar S, Jain NK, Paul CP (2014) Development of micro-plasma transferred arc (μ-PTA) wire deposition process for additive layer manufacturing applications. J Mater Process Technol 214:1102–1110. https://doi.org/10.1016/j.jmatprotec.2013.12.016
19. Jhavar S, Paul CP, Jain NK (2016) Micro-plasma transferred arc additive manufacturing for die and mold surface remanufacturing. JOM 68:1801–1809. https://doi.org/10.1007/s11837-016-1932-z
20. Kim S-Y, Park G-H, Kim H-A et al (2017) Micro-deposition of Cu-based metallic glass wire by direct laser melting process. Mater Lett 202:1–4. https://doi.org/10.1016/j.matlet.2017.05.092
21. Demir AG (2018) Micro laser metal wire deposition for additive manufacturing of thin-walled structures. Opt Lasers Eng 100:9–17. https://doi.org/10.1016/j.optlaseng.2017.07.003
22. Biffi CA, Tuissi A, Demir AG (2021) Martensitic transformation, microstructure and functional behavior of thin-walled Nitinol produced by micro laser metal wire deposition. J Market Res 12:2205–2215. https://doi.org/10.1016/j.jmrt.2021.03.108
23. Shaikh MO, Chen C-C, Chiang H-C et al (2019) Additive manufacturing using fine wire-based laser metal deposition. Rapid Prototyp J 26:473–483. https://doi.org/10.1108/RPJ-04-2019-0110
24. Dornelas PHG, Oliveira JP, da Silva TC et al (2024) Development of a gas metal arc based prototype for direct energy deposition with micrometric wire. J Market Res 30:3571–3583. https://doi.org/10.1016/j.jmrt.2024.04.056
25. Pickering FB (2006) High strength low alloy steels. Materials Science and Technology, Wiley
26. Lei YB, Wang ZB, Zhang B et al (2020) Enhanced mechanical properties and corrosion resistance of 316l stainless steel by preforming a gradient nanostructured surface layer and annealing. SSRN Electron J. https://doi.org/10.2139/ssrn.3692992
27. Rodrigues TA, Cipriano Farias FW, Avila JA et al (2023) Effect of heat treatments on Inconel 625 fabricated by wire and arc additive manufacturing: an in situ synchrotron X-ray diffraction analysis. Sci Technol Weld Joining 28:534–539. https://doi.org/10.1080/13621718.2023.2187927
28. Rodrigues TA, Cipriano Farias FW, Zhang K et al (2022) Wire and arc additive manufacturing of 316L stainless steel/Inconel 625 functionally graded material: development and characterization. J Market Res 21:237–251. https://doi.org/10.1016/j.jmrt.2022.08.169
29. Scotti A, Batista MA, Eshagh M (2022) Inaccuracy in arc power calculation through a product of voltage and current averages. J Braz Soc Mech Sci Eng 44:11. https://doi.org/10.1007/s40430-021-03317-6
30. Farias FWC, da Cruz Payão Filho J, Moraes e Oliveira VHP (2021) Prediction of the interpass temperature of a wire arc additive manufactured wall: FEM simulations and artificial neural network. Addit Manuf 48:102387. https://doi.org/10.1016/j.addma.2021.102387

31. Hielscher R, Schaeben H (2008) A novel pole figure inversion method: specification of the *MTEX* algorithm. J Appl Crystallogr 41:1024–1037. https://doi.org/10.1107/S0021889808030112
32. Oliver WC, Pharr GM (1992) An improved technique for determining hardness and elastic modulus using load and displacement sensing indentation experiments. J Mater Res 7:1564–1583. https://doi.org/10.1557/JMR.1992.1564
33. Lippold JC, Kotecki DJ (2005) Welding metallurgy and weldability of stainless steels
34. Suutala N (1983) Effect of solidification conditions on the solidification mode in austenitic stainless steels. Metall Trans A 14:191–197. https://doi.org/10.1007/BF02651615
35. Ragavendran M, Vasudevan M (2020) Laser and hybrid laser welding of type 316L(N) austenitic stainless steel plates. Mater Manuf Process 35:922–934. https://doi.org/10.1080/10426914.2020.1745231
36. Liverani E, Toschi S, Ceschini L, Fortunato A (2017) Effect of selective laser melting (SLM) process parameters on microstructure and mechanical properties of 316L austenitic stainless steel. J Mater Process Technol 249:255–263. https://doi.org/10.1016/j.jmatprotec.2017.05.042
37. Gowthaman PS, Jeyakumar S, Sarathchandra D (2023) Effect of heat input on microstructure and mechanical properties of 316l stainless steel fabricated by wire arc additive manufacturing. J Mater Eng Perform. https://doi.org/10.1007/s11665-023-08312-7
38. Wang C, Liu TG, Zhu P et al (2020) Study on microstructure and tensile properties of 316L stainless steel fabricated by CMT wire and arc additive manufacturing. Mater Sci Eng A 796:140006. https://doi.org/10.1016/j.msea.2020.140006
39. Wang D, Song C, Yang Y, Bai Y (2016) Investigation of crystal growth mechanism during selective laser melting and mechanical property characterization of 316L stainless steel parts. Mater Des 100:291–299. https://doi.org/10.1016/j.matdes.2016.03.111
40. Sun Z, Tan X, Tor SB, Yeong WY (2016) Selective laser melting of stainless steel 316L with low porosity and high build rates. Mater Des 104:197–204. https://doi.org/10.1016/j.matdes.2016.05.035
41. Röttger A, Boes J, Theisen W et al (2020) Microstructure and mechanical properties of 316L austenitic stainless steel processed by different SLM devices. Int J Adv Manuf Technol 108:769–783. https://doi.org/10.1007/s00170-020-05371-1
42. Hossein Nedjad S, Yildiz M, Saboori A (2023) Solidification behaviour of austenitic stainless steels during welding and directed energy deposition. Sci Technol Weld Join 28:1–17. https://doi.org/10.1080/13621718.2022.2115664
43. Abdali A, Hossein Nedjad S, Hamed Zargari H et al (2024) Predictive tools for the cooling rate-dependent microstructure evolution of AISI 316L stainless steel in additive manufacturing. J Market Res 29:5530–5538. https://doi.org/10.1016/j.jmrt.2024.03.008
44. Nagasai BP, Malarvizhi S, Balasubramanian V (2022) Mechanical properties and microstructural characteristics of wire arc additive manufactured 308 L stainless steel cylindrical components made by gas metal arc and cold metal transfer arc welding processes. J Mater Process Technol 307:117655. https://doi.org/10.1016/j.jmatprotec.2022.117655
45. Haldar N, Anand S, Datta S, Das A (2023) Microstructure and mechanical property characterization of wire arc additively manufactured SS308L built part: study of heat interaction phenomena. J Mater Eng Perform. https://doi.org/10.1007/s11665-023-08926-x
46. Le VT, Mai DS (2020) Microstructural and mechanical characteristics of 308L stainless steel manufactured by gas metal arc welding-based additive manufacturing. Mater Lett 271:127791. https://doi.org/10.1016/j.matlet.2020.127791
47. Ma C, Peng Q, Mei J et al (2018) Microstructure and corrosion behavior of the heat affected zone of a stainless steel 308L–316L weld joint. J Mater Sci Technol 34:1823–1834. https://doi.org/10.1016/j.jmst.2017.12.016
48. Farias FWC, Duarte VR, Felice IO et al (2023) In situ interlayer hot forging arc-based directed energy deposition of Inconel® 625: process development and microstructure effects. Addit Manuf 66:103476. https://doi.org/10.1016/j.addma.2023.103476
49. Elmer JW, Fisher K, Gibbs G et al (2022) Post-build thermomechanical processing of wire arc additively manufactured stainless steel for improved mechanical properties and reduction of crystallographic texture. Addit Manuf 50:102573. https://doi.org/10.1016/j.addma.2021.102573
50. Ribeiro Figueiredo A, de Azevedo LMB, da Cruz GF et al (2023) Effect of annealing twins, strain-recrystallization processing and δ-phase fraction on microtexture and evaluation of mechanical properties of nickel-based superalloy 718. Mater Sci Eng A 881:145341. https://doi.org/10.1016/j.msea.2023.145341
51. Farias FWC, dos Santos TJG, Oliveira JP (2024) Directed energy deposition + mechanical interlayer deformation additive manufacturing: a state-of-the-art literature review. Int J Adv Manuf Technol. https://doi.org/10.1007/s00170-024-13126-5
52. Gäumann M, Henry S, Cléton F et al (1999) Epitaxial laser metal forming: analysis of microstructure formation. Mater Sci Eng A 271:232–241. https://doi.org/10.1016/S0921-5093(99)00202-6
53. Gustafsson M, Thuvander M, Bergqvist E-L et al (2007) Effect of welding procedure on texture and strength of nickel based weld metal. Sci Technol Weld Joining 12:549–555. https://doi.org/10.1179/174329307X213800
54. Suwas S, Ray RK (2014) Crystallographic Texture of Materials. Springer, London
55. Eagar TW, Tsai NS (1983) Temperature fields produced by traveling distributed heat sources. Weld J 62:346–355
56. Dornelas PHG, da Payão Filho JC, Moraes e Oliveira VHP et al (2022) Influence of interpass temperature on the simulated HAZ of a clad API 5L X65 pipe joint welded with a gas metal arc. Weld World 66:213–226. https://doi.org/10.1007/s40194-021-01244-7
57. Dornelas PHG, da Payão Filho J, C, Moraes e Oliveira VHP, et al (2022) Effect of the interpass temperature on simulated heat-affected zone of gas metal arc welded API 5L X70 pipe joint. Int J Ad Manuf Technol 119:261–274. https://doi.org/10.1007/s00170-021-08261-2
58. Dornelas PHG, da Payão Filho JC, Moraes e Oliveira VHP et al (2021) Studying the influence of the interpass temperature on the heat-affected zone of an API 5L X65 steel welded pipe joint through computational and physical simulations. Int J Press Vessels Pip 194:104548. https://doi.org/10.1016/j.ijpvp.2021.104548
59. Dornelas PHG, da Payão Filho JC, Farias FWC et al (2022) Influence of the interpass temperature on the microstructure and mechanical properties of the weld metal (AWS A5.18 ER70S-6) of a narrow gap welded API 5L X70 pipe joint. Int J Press Vessels Pip 199:104690. https://doi.org/10.1016/j.ijpvp.2022.104690
60. Bang KS, Cha JH, Han KT, Jeong HC (2021) Effects of Al, Si and N Content on the Formation of M-A Constituent and HAZ Toughness of Ti-Containing Low-Carbon Steel. Mater Sci Forum 1016:42–49. https://doi.org/10.4028/www.scientific.net/MSF.1016.42
61. Bhadeshia H, Svensson L (1993) Modelling the Evolution of Microstructure in Steel Weld Metal. Math Model Weld Phenom 1:109–182
62. Rafieazad M, Ghaffari M, Vahedi Nemani A, Nasiri A (2019) Microstructural evolution and mechanical properties of a low-carbon low-alloy steel produced by wire arc additive manufacturing.

Int J Adv Manuf Technol 105:2121–2134. https://doi.org/10.1007/s00170-019-04393-8
63. Sun L, Jiang F, Huang R et al (2020) Anisotropic mechanical properties and deformation behavior of low-carbon high-strength steel component fabricated by wire and arc additive manufacturing. Mater Sci Eng A 787:139514. https://doi.org/10.1016/j.msea.2020.139514
64. López-Martínez E, Vázquez-Gómez O, Vergara-Hernández HJ et al (2016) Mechanical characterization of the welding of two experimental HSLA steels by microhardness and nanoindentation tests. Met Mater Int 22:987–994. https://doi.org/10.1007/s12540-016-6271-7
65. Stewart JL, Williams JJ, Chawla N (2012) Influence of thermal aging on the microstructure and mechanical behavior of dual-phase, precipitation-hardened, powder metallurgy stainless steels. Metall and Mater Trans A 43:124–135. https://doi.org/10.1007/s11661-011-0844-3
66. Guo LQ, Lin MC, Qiao LJ, Volinsky AA (2013) Ferrite and austenite phase identification in duplex stainless steel using SPM techniques. Appl Surf Sci 287:499–501. https://doi.org/10.1016/j.apsusc.2013.09.041
67. Kamaya M (2009) A procedure for estimating Young's modulus of textured polycrystalline materials. Int J Solids Struct 46:2642–2649. https://doi.org/10.1016/j.ijsolstr.2009.02.013
68. Tankova T, Andrade D, Branco R et al (2022) Characterization of robotized CMT-WAAM carbon steel. J Constr Steel Res 199:107624. https://doi.org/10.1016/j.jcsr.2022.107624
69. Ermakova A, Mehmanparast A, Ganguly S et al (2020) Investigation of mechanical and fracture properties of wire and arc additively manufactured low carbon steel components. Theoret Appl Fract Mech 109:102685. https://doi.org/10.1016/j.tafmec.2020.102685
70. Laghi V, Arrè L, Tonelli L et al (2023) Mechanical and microstructural features of wire-and-arc additively manufactured carbon steel thick plates. Int J Adv Manuf Technol 127:1391–1405. https://doi.org/10.1007/s00170-023-11538-3
71. Gordon JV, Haden CV, Nied HF et al (2018) Fatigue crack growth anisotropy, texture and residual stress in austenitic steel made by wire and arc additive manufacturing. Mater Sci Eng A 724:431–438. https://doi.org/10.1016/j.msea.2018.03.075
72. Zhao Y, Chen Y, Wang Z et al (2023) Mechanical properties, microstructural characteristics and heat treatment effects of WAAM stainless-steel plate material. J Build Eng 75:106988. https://doi.org/10.1016/j.jobe.2023.106988
73. Colin J, Fatemi A, Taheri S (2011) Cyclic hardening and fatigue behavior of stainless steel 304L. J Mater Sci 46:145–154. https://doi.org/10.1007/s10853-010-4881-x
74. Yoshinaga N, Sugiura N, Hiwatashi S (2017) A novel texture improving young's modulus in rolling direction of hot rolled low carbon sheet steel. ISIJ Int 57:2263–2265. https://doi.org/10.2355/isijinternational.ISIJINT-2017-372